INTERNATIONAL JOURNAL FOR NUMERICAL METHODS IN FLUIDS
Int. J. Numer. Meth. Fluids 2011; **67**:1358–1372
Published online 27 September 2010 in Wiley Online Library (wileyonlinelibrary.com). DOI: 10.1002/fld.2420

Numerical studies of the fingering phenomena for the thin film equation

Yibao Li[1], Hyun Geun Lee[1], Daeki Yoon[1], Woonjae Hwang[2], Suyeon Shin[1], Youngsoo Ha[3] and Junseok Kim[1,*,†]

[1]*Department of Mathematics, Korea University, Seoul 136-701, Republic of Korea*
[2]*Department of Information and Mathematics, Korea University, Jochiwon 339-700, Republic of Korea*
[3]*National Institute for Mathematical Science, Daejeon 305-340, Republic of Korea*

SUMMARY

We present a new interpretation of the fingering phenomena of the thin liquid film layer through numerical investigations. The governing partial differential equation is $h_t+(h^2-h^3)_x=-\nabla\cdot(h^3\nabla\Delta h)$, which arises in the context of thin liquid films driven by a thermal gradient with a counteracting gravitational force, where $h=h(x,y,t)$ is the liquid film height. A robust and accurate finite difference method is developed for the thin liquid film equation. For the advection part $(h^2-h^3)_x$, we use an implicit essentially non-oscillatory (ENO)-type scheme and get a good stability property. For the diffusion part $-\nabla\cdot(h^3\nabla\Delta h)$, we use an implicit Euler's method. The resulting nonlinear discrete system is solved by an efficient nonlinear multigrid method. Numerical experiments indicate that higher the film thickness, the faster the film front evolves. The concave front has higher film thickness than the convex front. Therefore, the concave front has higher speed than the convex front and this leads to the fingering phenomena. Copyright © 2010 John Wiley & Sons, Ltd.

Received 12 March 2010; Revised 11 August 2010; Accepted 11 August 2010

KEY WORDS: nonlinear diffusion equation; Marangoni stress; fingering instability; thin film; nonlinear multigrid method; finite difference

1. INTRODUCTION

Thin coating flows are of great technical, scientific, and industrial interest. Coating processes normally require an external driving force such as spinning to spread a liquid film along a solid substrate. For situations in which the substrate cannot be moved, surface forces can be manipulated to drive the spreading process. For example, thermal gradients provide a way to direct thin films into small crevices requiring lubrication. A liquid film supported on a substrate subject to a thermal gradient will experience a varying surface tension depending on the local temperature since colder regions maintain a higher surface tension than the warmer regions. This thermally induced Marangoni stress will force the liquid to spread [1]. In many situations, for example, spin coating process [2, 3], the fronts become unstable, leading to the formation of finger-like patterns, which is undesirable in technological applications. From a more fundamental point of view, one wishes to understand these strongly nonlinear fingering dynamics [4]. Thin film flows have been extensively studied experimentally [5, 6], analytically [1, 7–10], and numerically [11–26]. Karlsen and Lie [11] proposed an unconditionally stable scheme based on operator splitting combined with a front

*Correspondence to: Junseok Kim, Department of Mathematics, Korea University, Seoul 136-701, Republic of Korea.
†E-mail: cfdkim@korea.ac.kr

tracking method for a class of nonlinear parabolic equations. Sellier and Panda [12] described a first-order PDE with non-constant coefficients, which involves fourth-order derivatives of the desired free-surface profile and solved the first-order PDE using the method of characteristics. Ha *et al.* [13] presented a comparison of numerical schemes (Crank–Nicolson, fully implicit, Godunov, adapted upwind, and WENO schemes) for the convection term of a fourth-order thin film equation. An alternating direction implicit (ADI) scheme, which splits the n-dimensional problem into n one-dimensional implicit problems, has been used to solve the thin film equation [14–16]. This approach is a more popular alternative to explicit one, which is extremely restrictive in the choice of time step. Witelski and Bowen [15] constructed an ADI scheme for the solution of two-dimensional higher-order linear and nonlinear diffusion equations, particularly including the fourth-order thin film equation for surface tension-driven fluid flows. Myers *et al.* [16] solved the flow of a thin film, with and without solidification, on an arbitrary three-dimensional substrate by combining an ADI scheme with a shock capturing method. Recently, a multigrid approach has been developed as a more robust and efficient alternative to ADI scheme. Daniels *et al.* [17] showed that a fully implicit multigrid solver is more robust, returns an order of magnitude improvement in the rate of convergence, and requires low memory. Gaskell *et al.* applied a multigrid approach to droplet spreading flows [18] and continuous film flows with [19] or without [20] evaporation. Lee *et al.* [21] solved a thin film flow over a plane containing well-defined single and grouped topographic features using a full approximation storage (FAS) multigrid algorithm by employing automatic mesh adaptivity. Also the authors presented FILMPAR, which is a parallel multigrid algorithm for solving a three-dimensional gravity-driven continuous thin film free-surface flow over substrates containing micro-scale topography in [22]. Sellier *et al.* [23] used the multigrid and COMSOL solvers to solve the flow of thin liquid films on a plane surface containing occlusions. Veremieiev *et al.* [24] modelled an inertial thin film flow on inclined planar surfaces featuring topography via a depth-averaged form and solved using an FAS algorithm and a full multigrid (FMG) technique. Kim [25] developed an adaptive finite difference method for a class of fully nonlinear time-dependent thin liquid film equations. Kim and Sur [26] constructed a hybrid scheme that combines the essentially non-oscillatory (ENO) scheme for treating convection term and a nonlinear multigrid method for the diffusion term. For more details on the thin film equation, see the review paper [27] and the references therein. In this paper, we present a new interpretation of the mechanism of fingering phenomena by splitting the thin film equation into two parts: the advection part and diffusion part. It is the aim of this paper to investigate the mechanism of the fingering formation of the thin liquid film layer through numerical experiments.

This paper is organized as follows. In Section 2, we review the governing equation. In Section 3, the fully discrete, nonlinear FAS multigrid scheme for the thin film equation is given. In Section 4, we present numerical results. Conclusions are given in Section 5.

2. GOVERNING EQUATION

We consider the dynamics of a thin layer of liquid of thickness $h=h(x, y, t)$ on an inclined surface driven by thermally created surface tension gradients and influenced by gravity. The configuration is shown in Figure 1. The spatial variables x and y denote the direction of the flow and the direction normal to the flow, respectively. Let α, ρ, g, η, γ, and $\tau=\mathrm{d}\gamma/\mathrm{d}x$ denote the angle from horizontal inclination of the plane, the density, the gravitational constant, the dynamic viscosity, the surface tension, and the surface tension gradient of the liquid [27, 28], respectively.

We model the dynamics of the draining film using the lubrication approximation with a 'depth-averaged' velocity $\bar{\mathbf{u}}=(\bar{u}, \bar{v})$ [5, 24]:

$$\bar{u}=\frac{1}{h}\int_0^h u\,\mathrm{d}z=\frac{\tau h}{2\eta}-\frac{\rho g h^2\sin\alpha}{3\eta}+\frac{\gamma h^2\Delta h_x}{3\eta}-\frac{\rho g h^2 h_x\cos\alpha}{3\eta},$$

$$\bar{v}=\frac{1}{h}\int_0^h v\,\mathrm{d}z=\frac{\gamma h^2\Delta h_y}{3\eta}-\frac{\rho g h^2 h_y\cos\alpha}{3\eta}, \tag{1}$$

DOI: 10.1002/fld

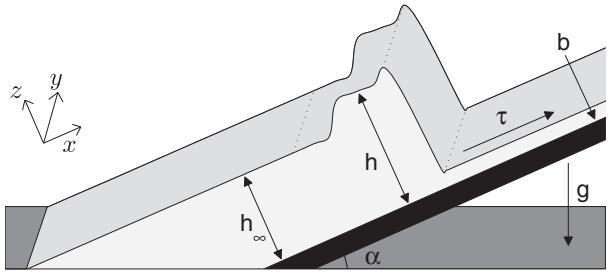

Figure 1. A schematic diagram of the physical problem. A thin layer of thickness h on an inclined surface driven by Marangoni stresses created by a temperature gradient on the plane. Gravity works against the stress to drive fluid back down the plane.

$$\bar{\mathbf{u}} = \left(\frac{\tau h}{2\eta} - \frac{\rho g h^2 \sin\alpha}{3\eta}\right)\vec{e}_x + \frac{\gamma h^2 \nabla \Delta h}{3\eta} - \frac{\rho g h^2 \nabla h \cos\alpha}{3\eta},$$

where $\vec{e}_x = (1, 0)$ and $\Delta = \nabla \cdot \nabla$ is the Laplacian operator. For example, from the experimental setting in [6], the surface tension gradient τ is taken as 0.11 Pa. In Equation (2), the first term is due to surface tension gradient, the second term is due to the tangential component of gravity, the third term is due to curvature, and the fourth term is due to the normal component of gravity. Coupling Equation (2) with mass conservation, we obtain

$$h_t + \nabla \cdot (h\bar{\mathbf{u}}) = 0. \tag{2}$$

To non-dimensionalize Equation (2), we employ the non-dimensional variables (denoted by hats)

$$h = H\hat{h}, \quad x = L\hat{x}, \quad y = L\hat{y} \quad \text{and} \quad t = T\hat{t}$$

to obtain

$$\frac{H}{T}\hat{h}_{\hat{t}} + \frac{1}{L}\hat{\nabla} \cdot \left[\left(\frac{H^2\tau\hat{h}^2}{2\eta} - \frac{H^3\rho g\hat{h}^3 \sin\alpha}{3\eta}\right)\vec{e}_x + \frac{H^4\gamma\hat{h}^3\hat{\nabla}\hat{\Delta}\hat{h}}{3L^3\eta} - \frac{H^4\rho g\hat{h}^3\hat{\nabla}\hat{h}\cos\alpha}{3L\eta}\right] = 0. \tag{3}$$

Now we define the characteristic variables by balancing terms. First we balance the tangential gravity and Marangoni terms to define H. Note that the independent and dependent variables are all of order 1. We obtain the following equation for H:

$$\frac{H^2\tau}{2\eta} = \frac{H^3\rho g \sin\alpha}{3\eta}, \quad \text{i.e. } H = \frac{3\tau}{2\rho g \sin\alpha}.$$

Next we define L such that the Marangoni and surface tension effects balance:

$$\frac{H^2\tau}{2\eta} = \frac{H^4\gamma}{3L^3\eta}, \quad \text{i.e. } L = \left(\frac{3\gamma\tau}{2\rho^2 g^2 \sin^2\alpha}\right)^{1/3}.$$

Now choose the time scale T so that gravity, Marangoni, and surface tension forces balance:

$$\frac{H}{T} = \frac{H^2\tau}{2L\eta}, \quad \text{i.e. } T = \frac{2\eta}{\tau^2}\left(\frac{4\gamma\tau\rho g \sin\alpha}{9}\right)^{1/3}.$$

We substitute the expressions for H, L, and T into Equation (3) and drop the '$\hat{}$' to obtain the dimensionless thin film equation:

$$h_t + (h^2 - h^3)_x = D\nabla \cdot (h^3\nabla h) - \nabla \cdot (h^3\nabla\Delta h),$$

DOI: 10.1002/fld

where $D=TH^3\rho g\cos\alpha/(3\eta L^2)$. Since an inclined plane is close vertical to the surface, we take $D=0$. Thus, we have derived the dimensionless thin film equation

$$h_t+(h^2-h^3)_x=-\nabla\cdot(h^3\nabla\Delta h). \tag{4}$$

This equation is a fourth-order nonlinear singular perturbation of the conservative law $h_t+(h^2-h^3)_x=0$ [28].

3. NUMERICAL METHOD

First, we split the fourth-order equation (4) into a system of second-order equations

$$h_t+f_x(h)=\nabla\cdot(M(h)\nabla\mu), \quad h=h(x,y,t), \tag{5}$$

$$\mu=-\Delta h \quad (x,y)\in\Omega=(0,L_x)\times(0,L_y), \quad t>0, \tag{6}$$

where $f(h)=h^2-h^3$ and $M(h)=h^3$. Boundary conditions are given by

$$h(0,y,t)=h_\infty, \quad h(L_x,y,t)=b, \quad h(x,0,t)=h(x,L_y,t),$$
$$\mu_x(0,y,t)=\mu_x(L_x,y,t)=0, \quad \mu(x,0,t)=\mu(x,L_y,t),$$

where h_∞ is a constant upstream height and b is a precursor film thickness.

3.1. Discretization of the proposed scheme

Now we present fully discrete schemes for Equations (5) and (6) in two-dimensional space. Let N_x and N_y be positive even integers, $\Delta x=(b-a)/N_x$ be the uniform mesh size, and $\Omega_{\Delta x}=\{(x_i,y_j): x_i=(i-0.5)\Delta x, y_j=(j-0.5)\Delta x, 1\leqslant i\leqslant N_x, 1\leqslant j\leqslant N_y\}$ be the set of cell-centers. Let h_{ij}^n and μ_{ij}^n be approximations of $h(x_i,y_j,n\Delta t)$ and $\mu(x_i,y_j,n\Delta t)$, respectively. Here $\Delta t=T/N_t$ is the time step, T is the final time, and N_t is the total number of time steps. Then, a semi-implicit time and centered difference space discretization of Equations (5) and (6) is

$$\frac{h_{ij}^{n+1}-h_{ij}^n}{\Delta t}=\nabla_d\cdot(M(h)_{ij}^{n+1}\nabla_d\mu_{ij}^{n+1})-f_x(h_{ij}^{n+1}), \tag{7}$$

$$\mu_{ij}^{n+1}=-\Delta_d h_{ij}^{n+1}, \tag{8}$$

where the superscripts denote discrete time steps. $f_x(h_{ij}^{n+1})$ is treated by using an implicit ENO-type scheme [29]. Since $f'(h)=2h-3h^2>0$ if $0<h<\frac{2}{3}$, we define

$$f_x(h_{ij}^{n+1}):=f'(h_{ij}^{n+1})\left(\frac{h_{ij}^{n+1}-h_{i-1,j}^{n+1}}{\Delta x}\right)+\Im(h_{ij}^n),$$

where $\Im(h^n)$ is computed as follows:

$$a=\frac{h_{ij}^n-h_{i-1,j}^n}{\Delta x}, \quad c=\frac{h_{i+1,j}^n-h_{ij}^n}{\Delta x}, \quad d_{ij}=\begin{cases}a & \text{if } |a|\leqslant|c|\\ c & \text{otherwise.}\end{cases}$$

Then we have $\Im(h_{ij}^n)=0.5(d_{ij}-d_{i-1,j})f'(h_{ij}^n)$. We define the boundary condition as

$$h_{0,j}=2h_\infty-h_{1,j}, \quad h_{N_x+1,j}=2b-h_{N_x,j}, \quad h_{i,0}=h_{i,N_y}, \quad h_{i,N_y+1}=h_{i,1},$$
$$\mu_{0,j}=\mu_{1,j}, \quad \mu_{N_x+1,j}=\mu_{N_x,j}, \quad \mu_{i,0}=\mu_{i,N_y}, \quad \mu_{i,N_y+1}=\mu_{i,1}.$$

We use a nonlinear FAS multigrid method to solve the nonlinear discrete system (7) and (8) at the implicit time level. A pointwise Gauss–Seidel relaxation scheme is used as the smoother in the multigrid method. See the reference text [30] for additional details and background. For a detailed description of the algorithm of the nonlinear multigrid method for solving the discrete system, please refer to References [21, 25, 26].

DOI: 10.1002/fld

4. NUMERICAL EXPERIMENTS

In this section, we perform numerical experiments such as efficiency and performance of multigrid solver, comparison of different advection schemes, role of the diffusion term in the thin film equation without the advection term, effect of h_∞, fingering instability, comparison with the experimental data, and long time evolution for the Marangoni-driven flow.

4.1. Efficiency of the multigrid solver

To investigate the efficiency of the multigrid method, we measure CPU times needed to solve the following problem:

$$h(x, y, 0) = 0.5[h_\infty + b - (h_\infty - b)\tanh(3(x-5) + \text{rand}(x, y))],$$

where $h_\infty = 0.175$ and $b = 0.002$. $2^n \times 2^{n-1}$ meshes are used on $\Omega = (0, 5\cdot 2^{n-3}) \times (0, 5\cdot 2^{n-4})$ for $n = 5, 6, 7, 8, 9$, and 10. Each calculation is run up to time $T = 50$ with a time step $\Delta t = 0.5$. Figure 2 shows CPU times versus the number of unknowns. The results fit a straight line. This implies that the multigrid solver achieves the $O(N)$ efficiency, where N is the number of unknowns.

4.2. Performance of smoothers and grid levels in the multigrid solver

In the multigrid method, a robust smoother is a necessary requirement to achieve grid-independent convergence. We compare the performance of Jacobi, Red–Black, and Gauss–Seidel relaxations as a smoother. The initial condition is

$$h(x, y, 0) = 0.5[h_\infty + b - (h_\infty - b)\tanh(3(x-2) + \text{rand}(x, y))], \tag{9}$$

where $h_\infty = 0.225$ and $b = 0.002$. A 64×64 mesh is used on $\Omega = (0, 10) \times (0, 10)$. Solutions are computed up to time $T = 10$ with a time step $\Delta t = 0.25$. Each iteration is run until the maximum error is less than 10^{-8}. Table I shows CPU times for three different relaxation schemes. We can see from Table I that the Gauss–Seidel method is the most efficient smoother.

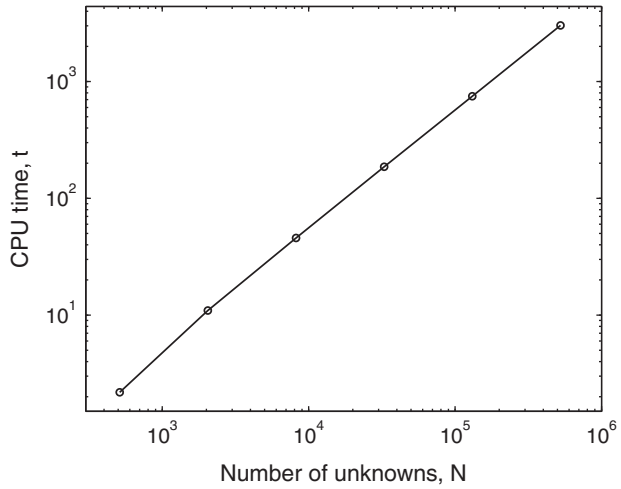

Figure 2. CPU time versus the number of unknowns. The multigrid solver achieves the $O(N)$ efficiency, where N is the number of unknowns.

Table I. CPU times for three different relaxation schemes.

Case	Jacobi	Red–Black	Gauss–Seidel
CPU time (s)	201.80	17.67	16.49

DOI: 10.1002/fld

Table II. CPU times for different coarse grid levels.

Case	V(3,3)	V(4,4)	V(5,5)	V(6,6)
CPU time (s)	109.516	71.60	72.14	72.31

Next, we compare the performance of coarse grid levels in the multigrid solver. The initial condition is given by Equation (9). A 128×128 mesh is used on $\Omega=(0,10)\times(0,10)$. We take $h_\infty=0.225$, $b=0.002$, $\Delta t=0.25$, and $T=10$. In this test, the experiment is performed using $(3,3)$, $(4,4)$, $(5,5)$, and $(6,6)$ V-cycles, where (v_1,v_2) indicates v_1 presmoothing and v_2 postsmoothing iterations. Note that we use the Gauss–Seidel relaxation in each V-cycle and each iteration is run until the maximum error is less than 10^{-8}. Table II shows CPU times for different coarse grid levels. With increasing number of grid levels from $V(4,4)$ to $V(6,6)$, we get only a slight increase of the CPU time. But, in the case of $V(3,3)$, many smoothings are required since the coarsest grid is not sufficiently coarse to solve the problem. This causes a dramatic increase in the CPU time. Therefore, we need sufficiently coarse grid levels to calculate fast.

4.3. *Stability test*: *comparison of different advection schemes*

Now, we test the stability of proposed scheme with explicit ENO, explicit upwind, and implicit upwind schemes for the advection term. For the diffusion term, we use the same implicit scheme. The initial condition in one dimension is

$$h(x,0)=0.5[h_\infty+b-(h_\infty-b)\tanh(3(x-10))],$$

where $h_\infty=0.3$ and $b=0.1$ (see the thick solid line in Figure 3(a)). A 1024 grid is used on $\Omega=(0,100)$. Solutions are computed up to time $T=200$ with different time steps. Figure 3 shows the stability of four different advection schemes. Figure 3(a) shows numerical solutions with four different schemes using a time step $\Delta t=0.1$. In Figure 3(b) (the close-up view of Figure 3(a)), the dotted, dashed, dash-dot, and solid lines are results with the explicit ENO, our proposed, explicit upwind, and implicit upwind schemes, respectively. As can be seen, all schemes seem well to describe the simulation of thin film by using a small time step, whereas Figure 3(c) shows numerical solutions with four different schemes using a slightly larger time step $\Delta t=0.75$. This result shows that the explicit ENO and explicit upwind schemes are unstable. Our proposed and implicit upwind schemes are stable. However, in the case of the implicit upwind scheme, the hump disappeared due to the numerical diffusion. Figure 3(d) shows numerical solutions with two different schemes using a time step $\Delta t=2.5$. The dotted and solid lines are results with our proposed and implicit upwind schemes, respectively. This result suggests that if we use a large time step, the hump disappeared due to the numerical diffusion. Therefore, to capture all phenomena of the solution, we need to use not only a fine grid but also a sufficiently small time step.

4.4. *Role of the diffusion term in the thin liquid film equation without the advection term*

Next, we consider the role of diffusion in the thin liquid film equation without the advection. The initial condition in one dimension is

$$h(x,0)=0.5[h_\infty+b-(h_\infty-b)\tanh(3(x-110))],$$

where $h_\infty=0.3$. The computational domain is $\Omega=(0,200)$. The uniform time step $\Delta t=100$ is used. Solutions are computed up to time $T=20000$. Figure 4(a) shows the evolutions of the thin film height h with the precursor film thickness $b=0.1$ and a grid size $N_x=1024$. In Figure 4(b), the stared and circled lines represent the evolutions of $h_{\max}-h_\infty$ and $b-h_{\min}$, respectively. Here, $h_{\max}=\max_{x\in\Omega}h(x)$ and $h_{\min}=\min_{x\in\Omega}h(x)$. They start at zero and converge quickly to constant values. Figures 4(c), (d), and (e) show the thin film heights at time $T=20000$ with different precursor film thicknesses $b=0.01$, 0.1, and 0.2 on three different grids, respectively. The stared, circled, and plused lines represent the results on different grids $N_x=256$, 512, and 1024,

DOI: 10.1002/fld

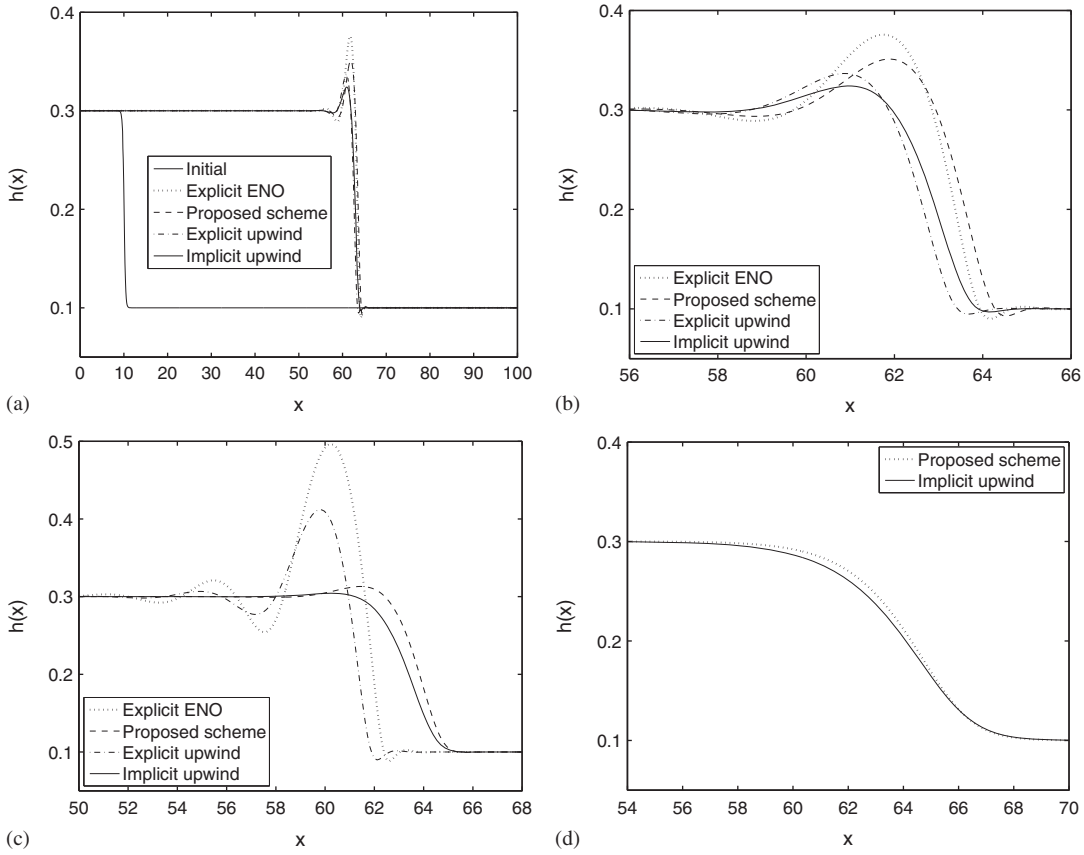

Figure 3. The evolutions with three different time steps: (a) and (b) using a small time step, all schemes are stable; (c) using a slightly larger time step, only our proposed and implicit upwind schemes are stable; and (d) however, in the case of the implicit upwind scheme, the hump disappeared due to the numerical diffusion. (a) $\Delta t = 0.1$; (b) a close-up view of (a); (c) $\Delta t = 0.75$; and (d) $\Delta t = 2.5$.

respectively. The results show the convergence as we refine the grids. Figure 4(f) shows $h_{\max} - h_\infty$ and $b - h_{\min}$ with different b values on the grids $N_x = 256$, 512, and 1024. This result shows that with fixed h_∞ value, $h_{\max} - h_\infty$ is decreasing and $b - h_{\min}$ is concave with respect to b.

Now, let us consider the numerical result with the precursor film thickness $b = 0.1$. In Figure 5, the dashed and circled lines represent $h(x, 50)$ and $-(h^3 h_{xxx})_x \times 50$ at $t = 50$, respectively. The bright gray region represents $-(h^3 h_{xxx})_x > 0$ and the dark gray region represents $-(h^3 h_{xxx})_x < 0$. Positive (or negative) value of $-(h^3 h_{xxx})_x$ implies that h_t is greater (or less) than zero, i.e., $h(x, t)$ will increase (or decrease). As predicted, in the bright gray region, $h(x, 100)$ increased than $h(x, 50)$ (see the solid line in Figure 5).

We also perform a similar numerical experiment in two dimensions with the following initial condition:

$$h(x, y, 0) = 0.5[h_\infty + b - (h_\infty - b)\tanh(3(x - 10) - 10\cos(\pi y/10))],$$

where $h_\infty = 0.3$ and $b = 0.01$. A 256×256 mesh is used on $\Omega = (0, 20) \times (0, 20)$. We take $\Delta t = 0.5$. Figures 6(a1), (a2), and (a3) show $h(x, y, t)$ at $t = 0$, 1, and 9, respectively. In Figures 6(b1), (b2), and (b3), filled contours of $-\nabla \cdot (h^3 \nabla \Delta h)$ are shown. The bright region represents $-\nabla \cdot (h^3 \nabla \Delta h) > 0$ and the dark region represents $-\nabla \cdot (h^3 \nabla \Delta h) < 0$. Positive and negative values of $-\nabla \cdot (h^3 \nabla \Delta h)$ imply that $h(x, y, t)$ will increase and decrease, respectively.

DOI: 10.1002/fld

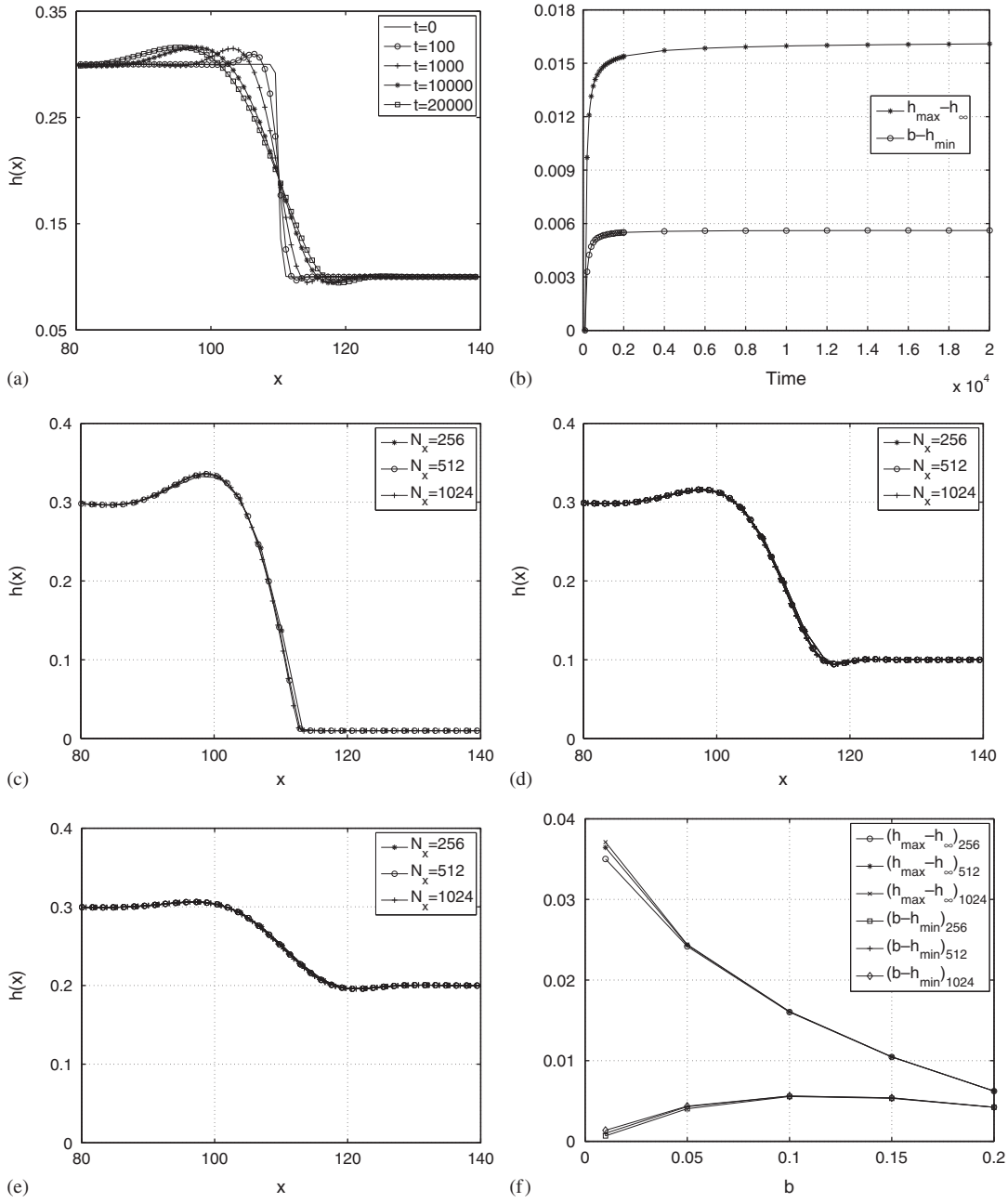

Figure 4. (a) The evolutions of the thin film height h with $b=0.1$ and $N_x=1024$; (b) the stared and circled lines represent evolutions of $h_{\max}-h_\infty$ and $b-h_{\min}$, respectively. (c), (d), and (e) show the thin film heights with $b=0.01$, 0.1, and 0.2 on the different grids, respectively; and (f) $h_{\max}-h_\infty$ and $b-h_{\min}$ with different b values on the grids. (c) $b=0.01$; (d) $b=0.1$; and (e) $b=0.2$.

4.5. Convection with non-convex flux, $f(h)=h^2-h^3$: the effect of h_∞

As shown in [28], Equation (4) has a single Lax shock solution

$$h(x,t)=\begin{cases} h_\infty & \text{if } x<st, \\ b & \text{if } x>st, \end{cases}$$

DOI: 10.1002/fld

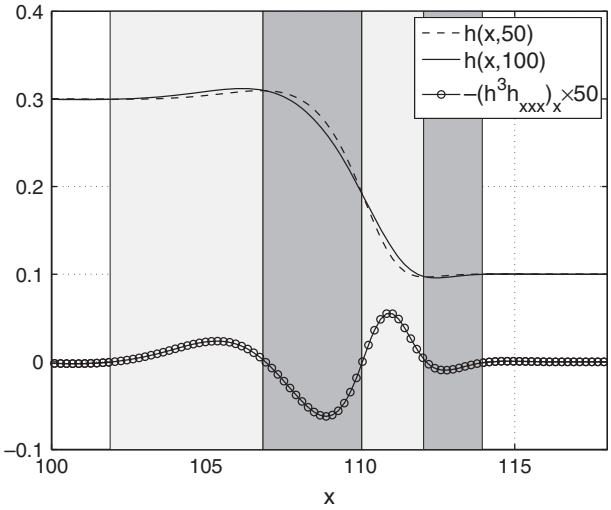

Figure 5. The bright gray region represents $-(h^3 h_{xxx})_x > 0$ and the dark gray region represents $-(h^3 h_{xxx})_x < 0$. Positive (or negative) value of $-(h^3 h_{xxx})_x$ implies that h_t is greater (or less) than zero, i.e. $h(x,t)$ will increase (or decrease).

where the shock speed s is given by

$$s = \frac{f(h_\infty) - f(b)}{h_\infty - b} = -h_\infty^2 + (1-b)h_\infty + b - b^2 = -\left(h_\infty - \frac{1-b}{2}\right)^2 + \frac{(1-b)(1+3b)}{4}. \qquad (10)$$

As we can see from Equation (10), the shock speed is an increasing function of h_∞ until $h_\infty = (1-b)/2$ (see Figure 7(a)). To confirm this numerically, we consider the shock speed with different h_∞ values. The initial condition in one dimension is

$$h(x,0) = 0.5[h_\infty + b - (h_\infty - b)\tanh(3(x-5))],$$

where $b = 0.05$. A 1024 grid is used on $\Omega = (0, 40)$. Solutions are computed up to time $T = 80$ with a time step $\Delta t = 0.5$. Figure 7(b) shows the evolutions of the film height with $h_\infty = 0.1$, 0.2, and 0.3. The result indicates that higher the film height, the faster the film front evolves.

4.6. Fingering instability

In this section, we study the effect of h_∞ on the finger shape for Marangoni-driven flow. The initial condition is

$$h(x,y,0) = 0.5[h_\infty + b - (h_\infty - b)\tanh(3(x-5) + \mathrm{rand}(x,y))],$$

where $b = 0.002$ and rand (x, y) is a random number in $[-1, 1]$. These perturbations model deviations from the straight front in the experiments. A 256×128 mesh is used on $\Omega = (0, 100) \times (0, 50)$. Solutions are run up to time $T = 600$ with a time step $\Delta t = 0.5$. Figures 8(a), (b), and (c) show the evolutions of the fluid front with different $h_\infty = 0.175$, 0.2, and (c) $h_\infty = 0.225$, respectively. The times are $t = 300$, 360, 450, and 600 from bottom to top. The results show that the speed of the fluid front is an increasing function of h_∞ until $h_\infty = (1-b)/2$. We note that the fingering phenomena occurs by two mechanisms. One is that the concave front has higher film height than the convex front and the other is that higher the film height, the faster the film front evolves. The first and second mechanisms were observed from the numerical experiments in Figures 6 and 7(b), respectively. By combination of these two effects, the fingering phenomenon happens.

DOI: 10.1002/fld

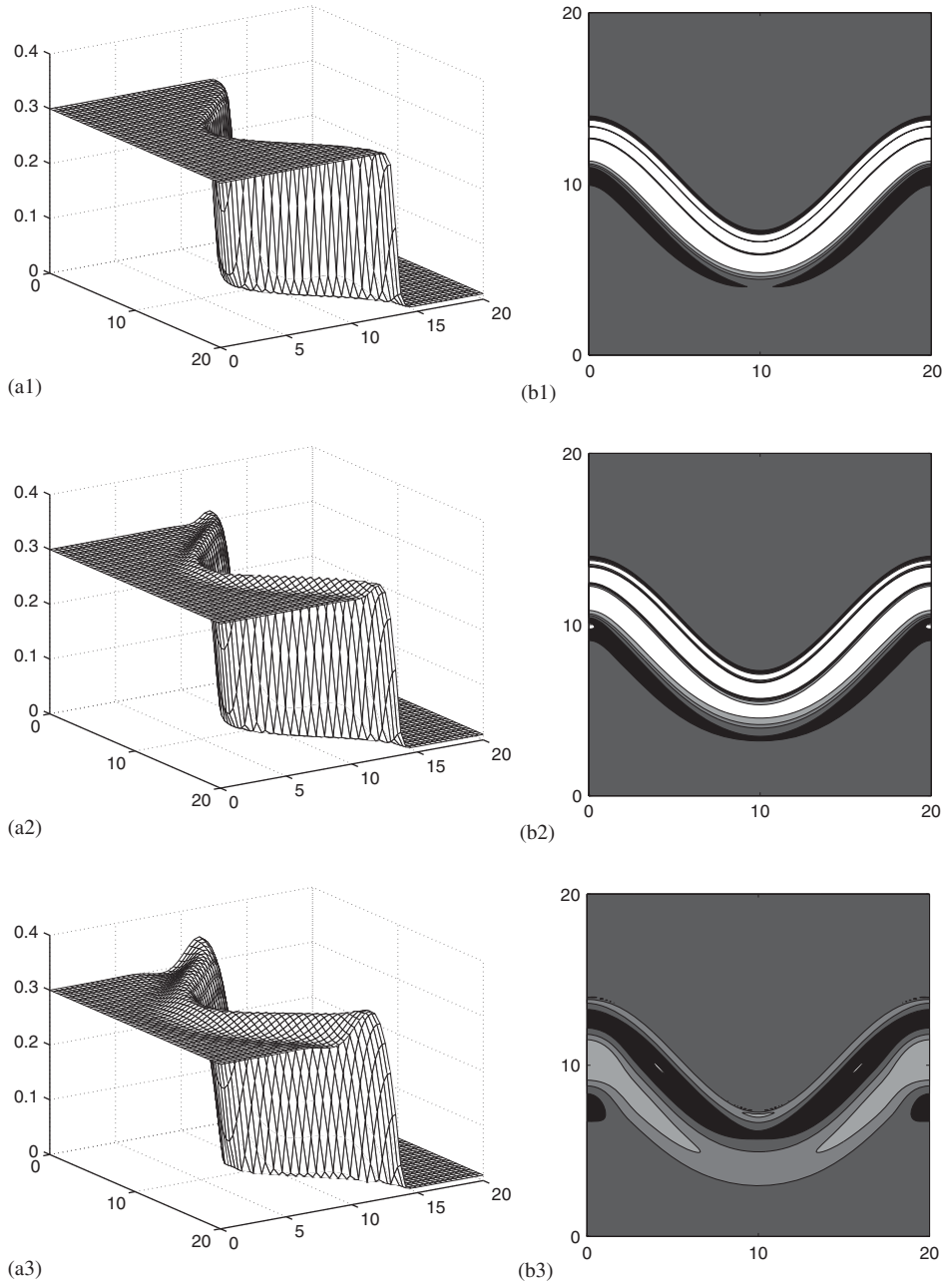

Figure 6. (a1)–(a3): the thin film height $h(x, y, t)$ at $t=0$, 1, and 9, respectively; (b1)–(b3): filled contours of $-\nabla\cdot(h^3\nabla\Delta h)$ at $t=0$, 1, and 9, respectively. The bright region represents $-\nabla\cdot(h^3\nabla\Delta h)>0$ and the dark region represents $-\nabla\cdot(h^3\nabla\Delta h)<0$.

4.7. Comparison with the experimental data

Next, we compare our results with two experimental data. We consider the thin film experiments that were performed by Sur *et al.* in [6]. In the first experiment, the initial condition is

$$h(x,0)=0.5[h_f+b-(h_f-b)\tanh(3(x-18))],$$

DOI: 10.1002/fld

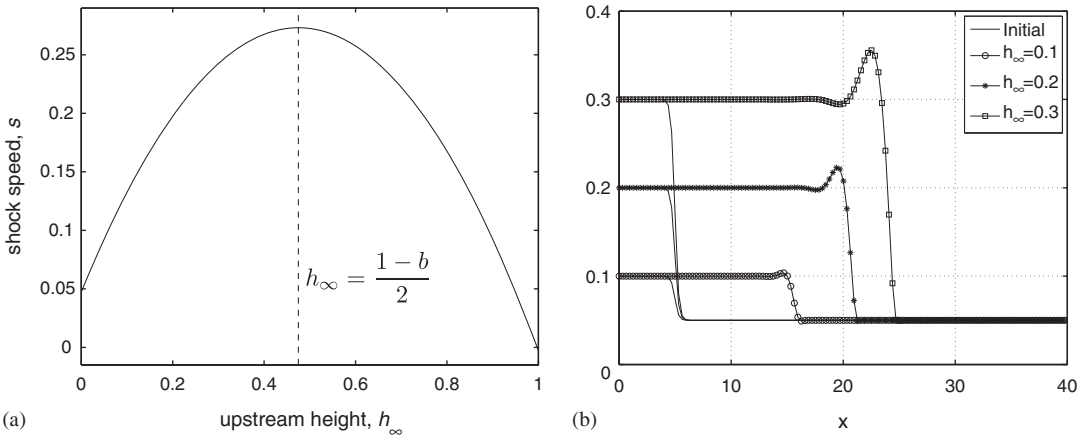

Figure 7. (a) The upstream height and shock speed and (b) the shock speed with different h_∞ values. Higher the film height, the faster the film front evolves.

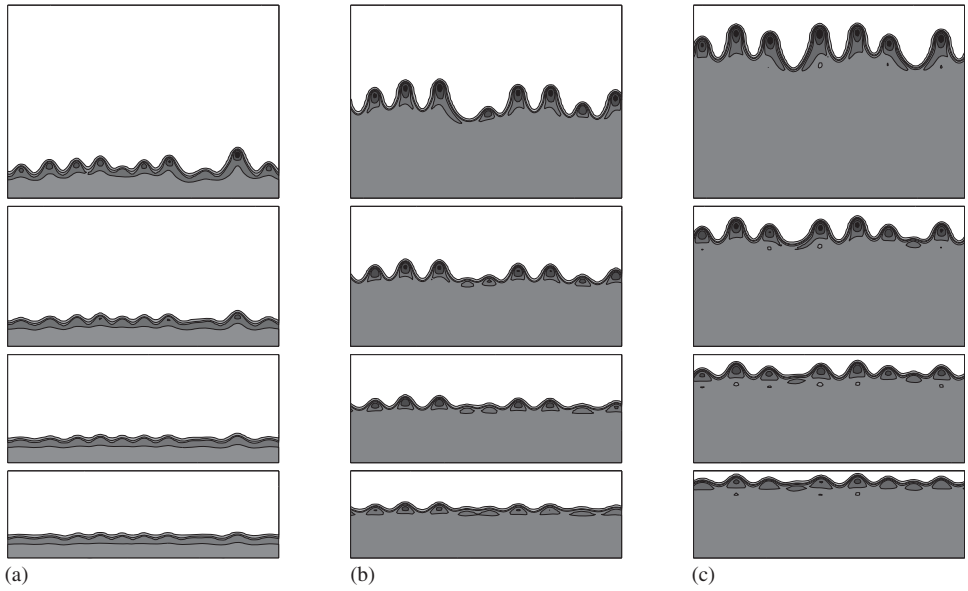

Figure 8. The effect of h_∞ on the finger shape for the Marangoni-driven flow. (a) $h_\infty = 0.175$; (b) $h_\infty = 0.20$; and (c) $h_\infty = 0.225$. The evolution of the fluid front is from bottom to top. The times are $t = 300$, 360, 450, and 600.

where $h_f = 0.75$, $h_\infty = 0.025$, and $b = 0.005$. A 1024 grid is used on $\Omega = (0, 50)$. Calculation is run up to time $T = 120$ with a time step $\Delta t = 0.05$. The result is shown in Figure 9(a). In the second experiment, the initial condition is

$$h(x, 0) = 0.5[h_f + b - (h_f - b)\tanh(3(x - 15.4))],$$

where $h_f = 0.75$, $h_\infty = 0.081$, and $b = 0.005$. A 512 grid is used on $\Omega = (0, 40)$. Calculation is run up to time $T = 75$ with a time step $\Delta t = 0.05$. The result is shown in Figure 9(b). These results show that our computational results are in qualitative agreement with experimental data.

4.8. Long-time evolution for Marangoni-driven flow

We perform a long-time evolution for Marangoni-driven flow. In [28], a reference frame moving with the speed of the front was used to locally reduce the numerical diffusion. To calculate a

DOI: 10.1002/fld

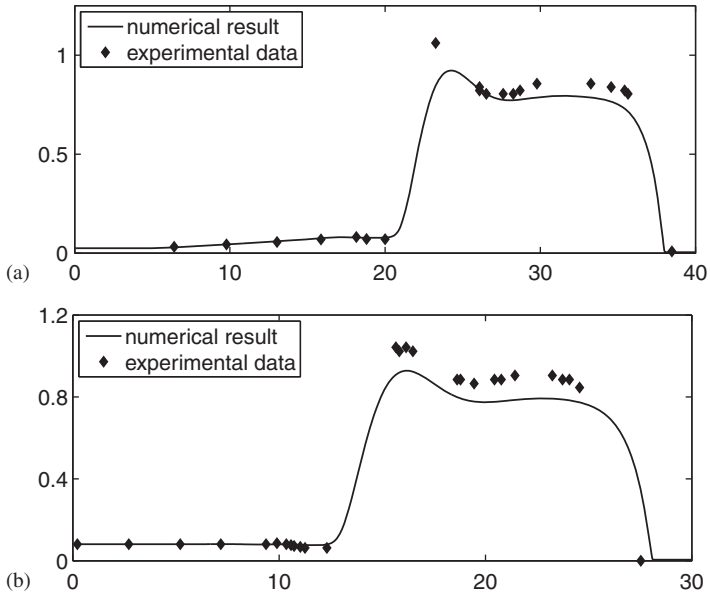

Figure 9. Comparison with the experimental data [6]. (a) $h(x,0)=0.5[h_f+b-(h_f-b)\tanh(3(x-18))]$, $h_f=0.75$, $h_\infty=0.025$, and $b=0.005$ and (b) $h(x,0)=0.5[h_f+b-(h_f-b)\tanh(3(x-15.4))]$, $h_f=0.75$, $h_\infty=0.081$, and $b=0.005$.

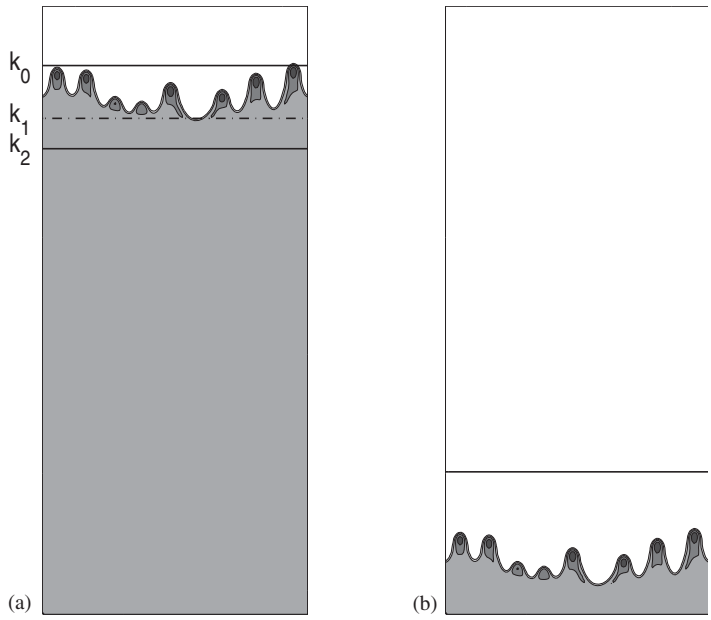

Figure 10. The proposed automatic shifting algorithm: (a) and (b) are before and after shifting, respectively.

long-time evolution, we designed a shifting mesh algorithm. The proposed automatic shifting algorithm is given in Appendix. Here we shifted the mesh when the front of the flow reached nine-tenths of the domain. The reason is that if we shift the mesh at early stage, then it is inefficient since we shifted the mesh although the flow can evolve more. And if we shift the mesh at late stage, then we cannot see correctly evolutions of the flow by the effect of the boundary condition b. And we did *Steps 1–2* when the maximum of the film height is greater than $(h_\infty+8b)/9$. Because if we consider that the maximum of the film height is greater than some position that is higher than

DOI: 10.1002/fld

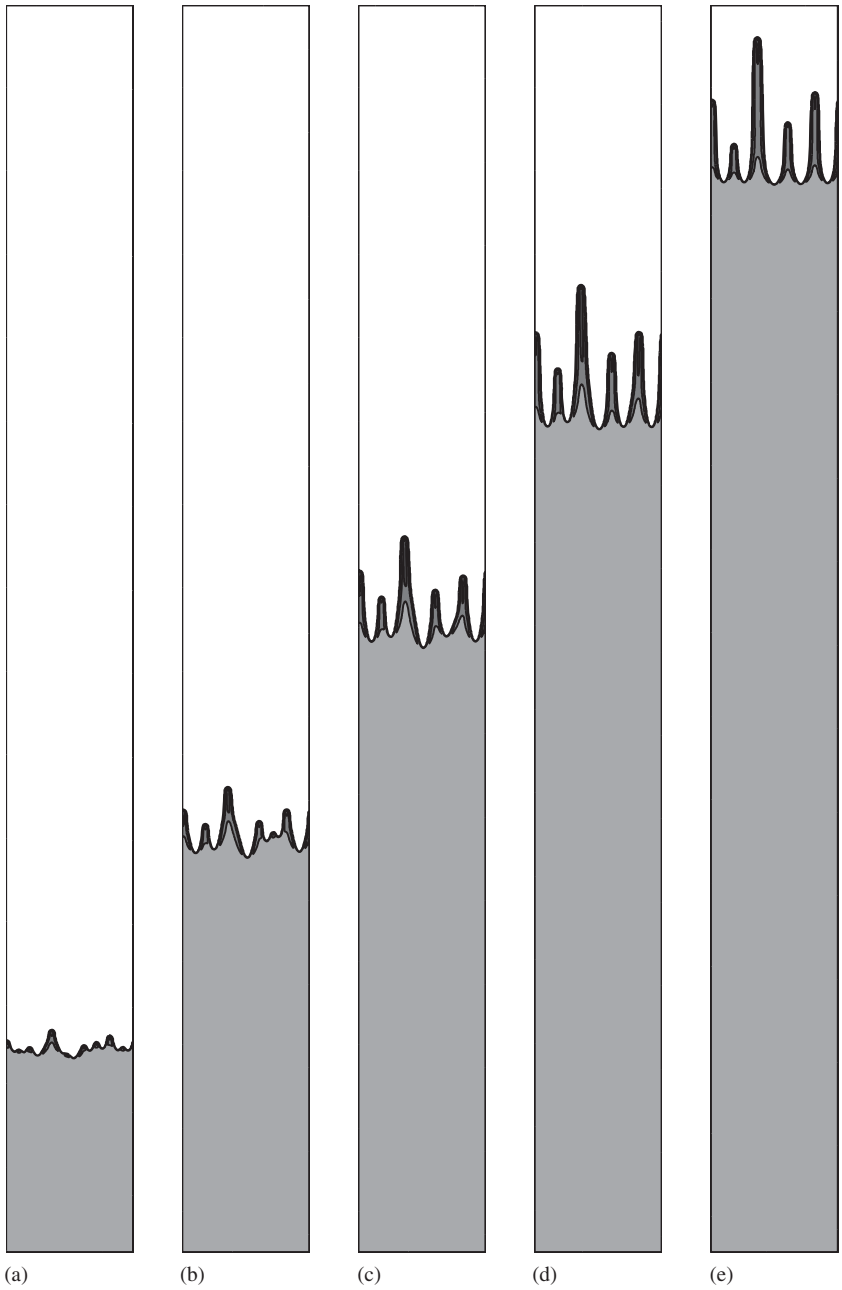

Figure 11. The finger shape for the Marangoni-driven flow at the following times: (a) $t=800$; (b) $t=1600$; (c) $t=2400$; (d) $t=3200$; and (e) $t=4000$. The effective domain size is $\Omega=(0,578)\times(0,50)$ and contours in 0.0019, 0.10, 0.15, 0.20, 0.25, 0.31, and 0.35, respectively.

$(h_\infty+8b)/9$, for example, $(h_\infty+4b)/5$, then it is too late to shift the mesh since the front of the flow can be influenced by the boundary condition b. The reason that we set $k_2=[k_1-0.05N_x]$ is to give sufficient mesh from h_∞ to hump region. Figure 10 shows the proposed automatic shifting algorithm. The initial condition is

$$h(x,y,0)=0.5[h_\infty+b-(h_\infty-b)\tanh(3(x-7)+\mathrm{rand}(x,y))],$$

DOI: 10.1002/fld

where $h_\infty = 0.175$ and $b = 0.002$. The computational domain using a spatial mesh of 256×128 is $\Omega = (0, 100) \times (0, 50)$. The uniform time step $\Delta t = 0.5$ is used. Figure 11 shows that the long-time evolution only took 3.34 h CPU time.

5. CONCLUSIONS

We presented a new interpretation of the fingering phenomena of the thin liquid film layer through numerical investigations. A robust and accurate finite difference method was developed for the thin liquid film equations. For the advection part $(h^2 - h^3)_x$, we used an implicit ENO-type scheme and got a good stability property. The resulting nonlinear discrete system was solved by an efficient nonlinear multigrid method. Numerical experiments indicated that higher the film thickness, the faster the film front evolves. The concave front has higher film thickness than the convex front. Therefore, the concave front has higher speed than the convex front and this leads to the fingering phenomena.

APPENDIX A

See the algorithm.

Algorithm:

Given an integer $k_0 = [0.9N_x]$ and a tolerance $tol = 10^{-5}$, where $[x]$ is the greatest integer not greater than x.

If $\left(\max_{1 \leqslant j \leqslant N_y} h_{k_0 j} > \frac{h_\infty + 8b}{9} \right)$

then do *Steps 1–2*

Step 1 Set $k_1 = k_0$

While $\left(\max_{1 \leqslant j \leqslant N_y} |\nabla_d h_{k_1 j}|^2 > tol \right)$ do

$k_1 = k_1 - 1$

End

Set $k_2 = [k_1 - 0.05N_x]$

Step 2 If $(1 \leqslant i \leqslant N_x - k_2 + 1$ and $1 \leqslant j \leqslant N_y)$

$\bar{h}_{ij} = h_{k_2 + i - 1, j}$

Else

$\bar{h}_{ij} = b$

End

We continue the calculation with $\bar{h}_{ij}$.

ACKNOWLEDGEMENTS

This research was supported by Basic Science Research Program through the National Research Foundation of Korea (NRF) funded by the Ministry of Education, Science and Technology (2008-C00044). The corresponding author (J. Kim) was also supported by a Korea University Grant.

REFERENCES

1. Kataoka DE, Troian SM. A theoretical study of instabilities at the advancing front of thermally driven coating films. *Journal of Colloid and Interface Science* 1997; **192**:350–362.
2. McKinley IS, Wilson SK, Duffy BR. Spin coating and air-jet blowing of thin viscous drops. *Physics of Fluids* 1999; **11**:30–47.

DOI: 10.1002/fld

3. Schwartz LW, Roy RV. Theoretical and numerical results for spin coating of viscous liquids. *Physics of Fluids* 2004; **16**:569–584.
4. Diez JA, Kondic L. Contact line instabilities of thin liquid films. *Physical Review Letters* 2001; **86**:632–635.
5. Bertozzi AL, Münch A, Fanton X, Cazabat AM. Contact line stability and 'undercompressive shocks' in driven thin film flow. *Physical Review Letters* 1998; **81**:5169–5172.
6. Sur J, Bertozzi AL, Behringer RP. Reverse undercompressive shock structures in driven thin film flow. *Physical Review Letters* 2003; **90**:126105-1–126105-4.
7. Bertozzi AL, Brenner MP. Linear stability and transient growth in driven contact lines. *Physics of Fluids* 1997; **9**:530–539.
8. Khayat RE, Kim K-T, Delosquer S. Influence of inertia, topography and gravity on transient axisymmetric thin-film flow. *International Journal for Numerical Methods in Fluids* 2004; **45**:391–419.
9. Spaid MA, Homsy GM. Stability of Newtonian and viscoelastic dynamic contact lines. *Physics of Fluids* 1996; **8**:460–478.
10. Troian SM, Herbolzheimer E, Safran SA, Joanny JF. Fingering instability of driven spreading films. *Europhysics Letters* 1989; **10**:25–30.
11. Karlsen KH, Lie K-A. An unconditionally stable splitting for a class of nonlinear parabolic equations. *IMA Journal of Numerical Analysis* 1999; **19**:609–635.
12. Sellier M, Panda S. Beating capillarity in thin film flows. *International Journal for Numerical Methods in Fluids* 2010; **63**:431–448.
13. Ha Y, Kim Y-J, Myers TG. On the numerical solution of a driven thin film equation. *Journal of Computational Physics* 2008; **227**:7246–7263.
14. Christov CI, Pontes J, Walgraef D, Velarde MG. Implicit time-splitting for fourth-order parabolic equations. *Computer Methods in Applied Mechanics and Engineering* 1997; **148**:209–224.
15. Witelski TP, Bowen M. ADI schemes for higher-order nonlinear diffusion equations. *Applied Numerical Mathematics* 2003; **45**:331–351.
16. Myers TG, Charpin JPF, Chapman SJ. The flow and solidification of a thin fluid film on an arbitrary three-dimensional surface. *Physics of Fluids* 2002; **14**:2788–2803.
17. Daniels N, Ehret P, Gaskell PH, Thompson HM, Decré M. Multigrid methods for thin liquid film spreading flows. *Proceedings of the First International Conference on Computational Fluid Dynamics*. Springer: Berlin, 2001; 279–284.
18. Gaskell PH, Jimack PK, Sellier M, Thompson HM. Efficient and accurate time adaptive multigrid simulations of droplet spreading. *International Journal for Numerical Methods in Fluids* 2004; **45**:1161–1186.
19. Gaskell PH, Jimack PK, Sellier M, Thompson HM, Wilson MCT. Gravity-driven flow of continuous thin liquid films on non-porous substrates with topography. *Journal of Fluid Mechanics* 2004; **509**:253–280.
20. Gaskell PH, Jimack PK, Sellier M, Thompson HM. Flow of evaporating, gravity-driven thin liquid films over topography. *Physics of Fluids* 2006; **18**:031601-1–031601-14.
21. Lee YC, Thompson HM, Gaskell PH. An efficient adaptive multigrid algorithm for predicting thin film flow on surfaces containing localised topographic features. *Computers and Fluids* 2007; **36**:838–855.
22. Lee YC, Thompson HM, Gaskell PH. FILMPAR: a parallel algorithm designed for the efficient and accurate computation of thin film flow on functional surfaces containing micro-structure. *Computer Physics Communications* 2009; **180**:2634–2649.
23. Sellier M, Lee YC, Thompson HM, Gaskell PH. Thin film flow on surfaces containing arbitrary occlusions. *Computers and Fluids* 2009; **38**:171–182.
24. Veremieiev S, Thompson HM, Lee YC, Gaskell PH. Inertial thin film flow on planar surfaces featuring topography. *Computers and Fluids* 2010; **39**:431–450.
25. Kim J. Adaptive mesh refinement for thin-film equations. *Journal of the Korean Physical Society* 2006; **49**: 1903–1907.
26. Kim J, Sur J. A hybrid method for higher-order nonlinear diffusion equations. *Communications of the Korean Mathematical Society* 2005; **20**:179–193.
27. Craster RV, Matar OK. Dynamics and stability of thin liquid films. *Reviews of Modern Physics* 2009; **81**: 1131–1198.
28. Bertozzi AL, Münch A, Shearer M. Undercompressive shocks in thin film flows. *Physica D* 1999; **134**:431–464.
29. Shu CW, Osher S. Efficient implementation of essentially non-oscillatory shock capturing schems II. *Journal of Computational Physics* 1989; **83**:32–78.
30. Trottenberg U, Oosterlee C, Schüller A. *Multigrid*. Academic Press: London, 2001.

DOI: 10.1002/fld